Boise State University

ScholarWorks

12-2015

Infrasound from Volcanic Rockfalls

Jeffrey B. Johnson
Boise State University

Timothy J. Ronan
University of North Carolina

Infrasound from volcanic rockfalls

Jeffrey B. Johnson[1] and Timothy J. Ronan[1,2]

[1]Department of Geosciences, Boise State University, Boise, Idaho, USA, [2]Department of Geological Sciences, University of North Carolina, Chapel Hill, USA

Abstract Proximal infrasound arrays can robustly track rapidly moving gravity-driven mass wasting, which occurs commonly at erupting volcanoes. This study reports on detection, localization, and quantification of frequent small rockfalls and infrequent pyroclastic density currents descending the southeast flanks of Santiaguito's active Caliente Dome in January of 2014. Such activities are identified as moving sources, which descend several hundred meters at bulk flow speeds of up to ~10 m/s, which is considerably slower than the descent velocity of individual blocks. Infrasound rockfall signal character is readily distinguishable from explosion infrasound, which is manifested by a relatively fixed location source with lower frequency content. In contrast, the rockfalls of Santiaguito possess higher frequencies dominated by 7.5 to 20 Hz energy. During our observation periods typical rockfall signals occurred ~10 times per hour and lasted tens of seconds or more. Array beamforming permitted detection of rockfall transients with amplitudes of only a few tens of millipascals that would be impossible to distinguish from noise using a single sensor. Conjoint time-synchronized video is used to corroborate location and to characterize various gravity-driven events.

1. Introduction

Infrasound is commonly used to study and monitor eruption dynamics and has proven effective for characterizing the style, intensity, and chronology of explosive eruption sequences [*Fee and Matoza*, 2013; *Johnson and Ripepe*, 2011]. Few infrasound studies, however, have focused on the identification and parameterization of volcano gravity-driven flows occurring on the volcanic edifice. Previous infrasound study of moving volcanic sources focused on block-and-ash flows at Unzen (Japan) [*Oshima and Maekawa*, 2001; *Yamasato*, 1997], rockfall at Mount St. Helens (United States) [*Moran et al.*, 2008], lahars at Villarrica (Chile) [*Johnson and Palma*, 2015], and pyroclastic flow activity at Soufrière Hills (Montserrat) [*Delle Donne et al.*, 2014; *Ripepe et al.*, 2009]; however, the identification and tracking of small rockfall signals, which occur commonly at active volcanoes, has not been the subject of extensive study.

Infrasonic identification of small rockfalls at volcanoes has been a challenge because typical volcano infrasound deployment topologies involve microphones located several kilometers or more from the source, and furthermore, sensors are often distributed in network configurations [e.g., *Fee et al.*, 2014; *Jones and Johnson*, 2011; *Cannata et al.*, 2009]. At these farther distances arrays have proven more effective for identifying small signal and tremors [e.g., *Yokoo et al.*, 2014; *Matoza et al.*, 2006; *Garces et al.*, 2003]; however, distal array placement can limit location resolution of moving sources. Distinction between near-vent tremor and potential rockfall signals, based upon waveform shape, may also be ambiguous.

Though seismic rockfall signal is routinely identified at volcanoes [*Hibert et al.*, 2011; *Jolly et al.*, 2002; *Norris*, 1994], infrasound rockfall tends to produce relatively small amplitude signals [*Moran et al.*, 2008; *Luckett et al.*, 2002], which often are obscured by background noise due to winds. Analyses of low signal-to-noise infrasound require the implementation of arrays, which use beamforming to pull signal from noise [*Olson and Szuberla*, 2008]. This study targets the dynamics of small gravity-driven flows using an array deployed within a kilometer of the vent of Volcán Santiaguito (Guatemala). We demonstrate the capabilities for infrasound monitoring to quantify the occurrence of rockfalls, track their movement, and distinguish these sources from degassing or explosion infrasound.

2. Background

Regular explosions produced by the andesitic-dacite Santiaguito dome generate kilometer high columns [e.g., *Bluth and Rose*, 2004], which produce characteristic and relatively high signal-to-noise infrasound transients [e.g., *Johnson and Lees*, 2010; *Johnson et al.*, 2014]. Episodic explosive activity occurring approximately
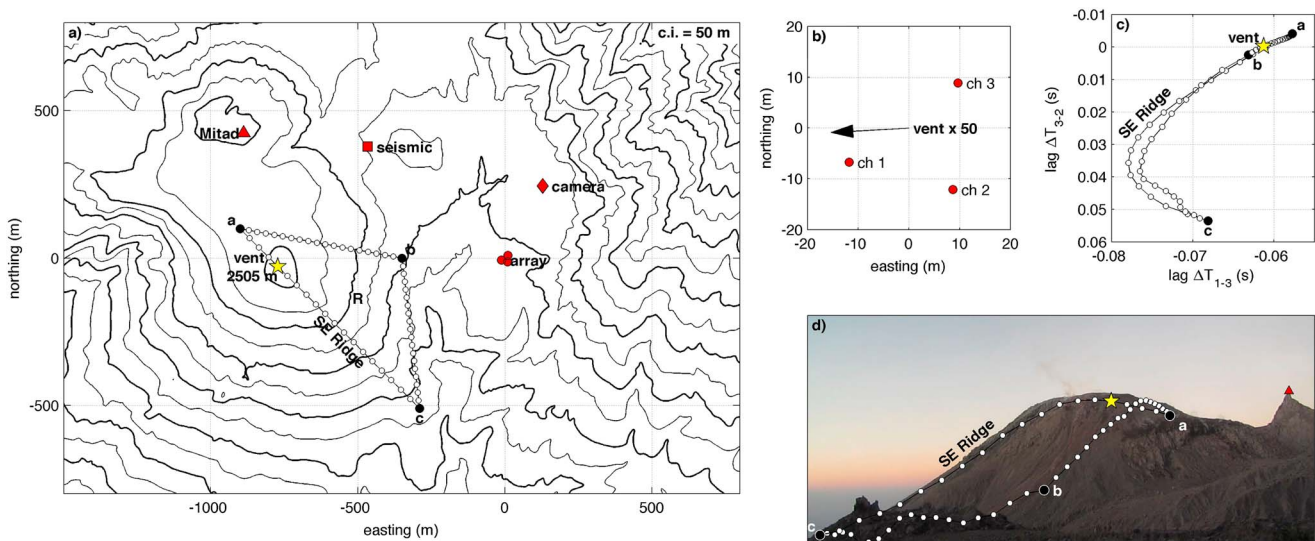
Figure 1. (a) Map showing location of infrasound array along with seismometer site and camera location. Yellow star indicates Caliente summit vent, and red triangle shows location of the inactive Mitad dome. Bounded triangular region (*R*) corresponds to rockfall and explosion search area as described in the text. The southeast ridge lies along the segment between the vent and vertex *c*. (b) Detail of sensor distribution in the array. Arrow indicates direction to vent and is drawn with length scaled to 1/50 of the vent-receiver distance. (c) Predicted acoustic lag times between channels 2 and 1 and channels 3 and 2 for sources located around the periphery of region *R* indicated in Figures 1a and 1d. (d) Triangular search region *R* and Mitad summit projected on to still image as seen from the camera site. Projection of digital elevation model on to video image frames is discussed in Appendix C.

10 times per day and coincident effusion of lava have been stable characteristics of Santiaguito's Caliente Dome since at least the 1970s [*Rose*, 1987]. Rockfall and small pyroclastic density currents can be induced by explosions, but rockfalls also occur spontaneously due to spalling from the blocky flow front.

These rockfalls, composed of blocks as large as 10 m, descend the steep-sided Caliente dome on southeast, south, and southwest aspects. During periods of high lava effusion (e.g., on the order of 1 m³/s [*Harris et al.*, 2003]) the lava flows extend continuously several kilometers from vent down to flatter terrain. During cyclic ebbs in effusion, the lava flow becomes discontinuous as it overflows the summit plateau and large blocks break and tumble from the flow scarp. In January 2014, during relatively moderate lava effusion (<1 m³/s), the flow was pouring over southeast aspects of the Caliente dome and comprised 10 m scarps some 50 to 100 m below the Caliente summit. Lava blocks routinely broke from these scarps, to roll and bounce downhill, giving rise to trails of ash easily visible from several kilometers. Blocks rolled as far as 700 m before reaching more moderate slopes and/or falling in to the incised gorge of the upper Rio Nima 2.

3. Study

In January 2014 we deployed a temporary infrasound array within 1 km of the regular rockfalls occurring at Santiaguito. The tripartite ~20 m aperture array was situated on a flat expanse ~900 m east and 200 m below the active vent and within line of sight to the east and southeast flanks (Figure 1). Its position was chosen to maximize azimuthal resolution of moving sources that commonly descend from the vent toward the southeast.

The three-element microphone array consisted of infraBSU 0.5 inch sensors linked with ~15 m cables to a DataCube 24 bit data logger sampling at 100 Hz. These sensors responded to pressure transients with flat sensitivity between 0.05 Hz and 50 Hz Nyquist and with a noise floor estimated at less than 5 mPa in the near-infrasound 1–20 Hz band [*Marcillo et al.*, 2012]. Data were recorded for 42 h between 12 January at 00:00 UTC (i.e., 11 January at 6:00 P.M. local time) until 13 January at 18:00 UTC (i.e., 12:00 P.M. local time).

Synchronous seismic recordings were made with a Guralp CMG 40-T seismometer (~30 s corner) and DataCube logger situated ~500 m northeast of the vent. This location reoccupied a locale used during previous field campaigns [e.g., *Johnson et al.*, 2014]. Seismic signal provides a record of both explosion and rockfall transients, but the single seismometer gave no reliable constraints on their source locations.

Additionally, a Canon Powershot SX260 HS camera was temporarily deployed some ~1000 m from the vent and configured to acquire continuous high-definition video (1920×1080 pixels) using the Canon Hack Development Kit (CHDK) software. The camera operated during periods of good visibility for 80 min on 12 January (6:40 to 8:00 A.M. local time) and for 270 min on 13 January (6:30 to 11:00 A.M. local time). Angular field of view was 32° on 12 January and 60° on 13 January. During processing the video was decimated to 1 Hz images and used to understand the relation between infrasound signal and physical sources occurring on the volcano.

4. Analysis

This study uses the array of three infrasound sensors to first identify infrasound signal (see Appendix A) and then calculate the most likely source location of that infrasound within a restricted search space (see Appendix B). The search space R comprises both the summit/vent region and the east and southeast slopes, where rockfalls routinely descend. The region R was predominantly within line of sight of the three-element array (Figures 1a and 1d).

A 30 min example of Santiaguito activity is shown in Figure 2. Both explosion and rockfall events are clearly evident during this time interval in both seismic (Figure 2a) and infrasound (Figure 2b) records. Processing described in this section, and in the appendices, permits distinction and localization of explosion and rockfall. The waveforms are analyzed for overlapping 5 s (500 sample) windows. Signal parameters presented herein, including spectral character and signal correlation, are resolved at 1 s time steps and use 4 s of overlap.

To quantify infrasound signal quality and its spectral content, we compute a *signal-to-noise ratio* (*SNR*) *spectrogram* as a function of frequency f and start time t (Figure 2e).

$$\text{SNR}(t,f) = P(t,f)/N(f). \qquad (1)$$

The SNR is calculated as the power spectrogram $P(t,f)$ of the data normalized by a noise spectral density estimate $N(f)$, which is analogous to the *base level noise seismic spectrum* of *Vila et al.* [2006]. Background noise spectrum quantification is subjective. We calculate it here as the mean value of the lowest vigintile (5%) power for hour-long infrasound spectrograms.

The resultant SNR spectrogram is particularly useful because it characterizes the frequency content of signals (e.g., rockfall or explosion), as opposed to a traditional infrasound spectrogram, which is a combination of signal and noise. A frequency-integrated SNR (Figure 2d) provides a measure of signal energy over time:

$$\text{snr}(t) = \int\limits_{0}^{50} \text{SNR}(t,f)\mathrm{d}f. \qquad (2)$$

Both *SNR(t, f)* and snr(t) are only displayed for time series that are considered signal as described in Appendix A. In Figure 2 SNR and snr possess highest amplitudes for the events occurring at 19:32 and 19:49, which are nonmoving explosion sources located within an ~100 m radius of the Caliente summit (see Appendix B). The explosion infrasound locations can vary spatially due to the extensive size of Caliente's venting region [*Jones and Johnson*, 2011]. Lower amplitude infrasound events are commonly associated with moving sources, which locate at varying distance to the southeast of the summit.

The SNR spectrum is also synthesized as a single time-varying value by considering its spectral centroid $f_c(t)$, which provides a measure of the weighted mean spectrum for a particular time window. The centroid SNR frequency indicated in Figure 2e is defined as follows:

$$f_c(t) = \frac{\int\limits_{0}^{50} f \times \text{SNR}(t,f)\mathrm{d}f}{\int\limits_{0}^{50} \text{SNR}(t,f)\mathrm{d}f}. \qquad (3)$$

5. Results

5.1. Moving and Nonmoving Sources and Their Spectral Character

Spectral synthesis coupled with inferred source locations is used to distinguish rockfall events from explosions for all signal in the catalog. At first inspection, moving and nonmoving sources are easily distinguished in the
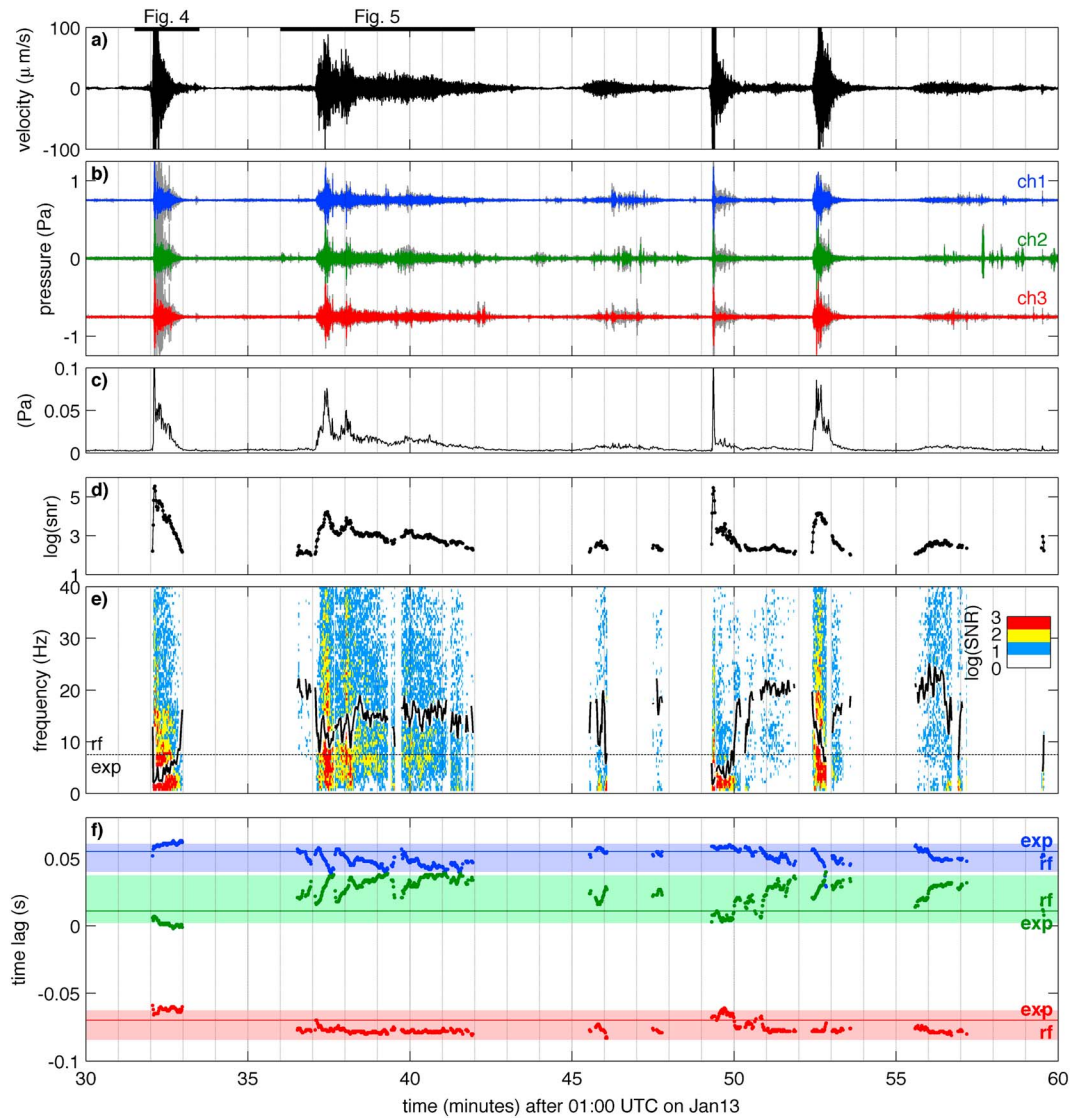
Figure 2. Thirty minute record sequence consisting of both explosions and rockfall. (a) Broadband unfiltered seismic signal. (b) Three channels of infrasound signal filtered above 1 Hz (gray) and within a limited 4–24 Hz band (colored waveforms). (c) One second decimated absolute pressure amplitudes of the 4–24 Hz infrasound; data are displayed from the lowest-amplitude channel recordings to minimize potential contributions of wind noise. (d) snr value for 5 s window and (e) SNR spectrogram along with centroid frequency (black line). SNR is calculated for 0.5 Hz wide frequency bins with center frequencies of $f = \{0.25, 0.75, 1.25, \ldots, 49.75\}$ Hz. (f) Cross-correlogram time series showing evolving time lags between peak correlated phases of the three station pairs. Transparent color bands show range of expected intersensor time lags for points confined to the triangular search region R in Figure 1. Domains of time lags associated with explosions (exp) and rockfalls (rf) are indicated.

evolving cross-correlation time lags of Figure 2f. These "cross-correlogram" time series indicate the evolving phase lags, which correspond to maximum cross-correlation values for the three unique station pairs. As with spectrograms, these time lags were determined as a function of t for overlapping 5 s time windows. These time lags are only shown for signal, which is defined as highly correlated and internally consistent (described in Appendix A). Those events that show systematic lag time evolution (e.g., 19:36 to 19:42 in Figure 2f) relate to moving sources, which cause sound to propagate across the array with systematically varying azimuth. These moving sources are consistently located on the steep southeast slopes of Caliente.

Time lags of infrasound signal crossing the array are used to map time-varying source locations as described in Appendix B. These locations correspond to the minimum timing residual between cross-correlation lag times and predicted time delays computed for candidate source locations on the surface of the active
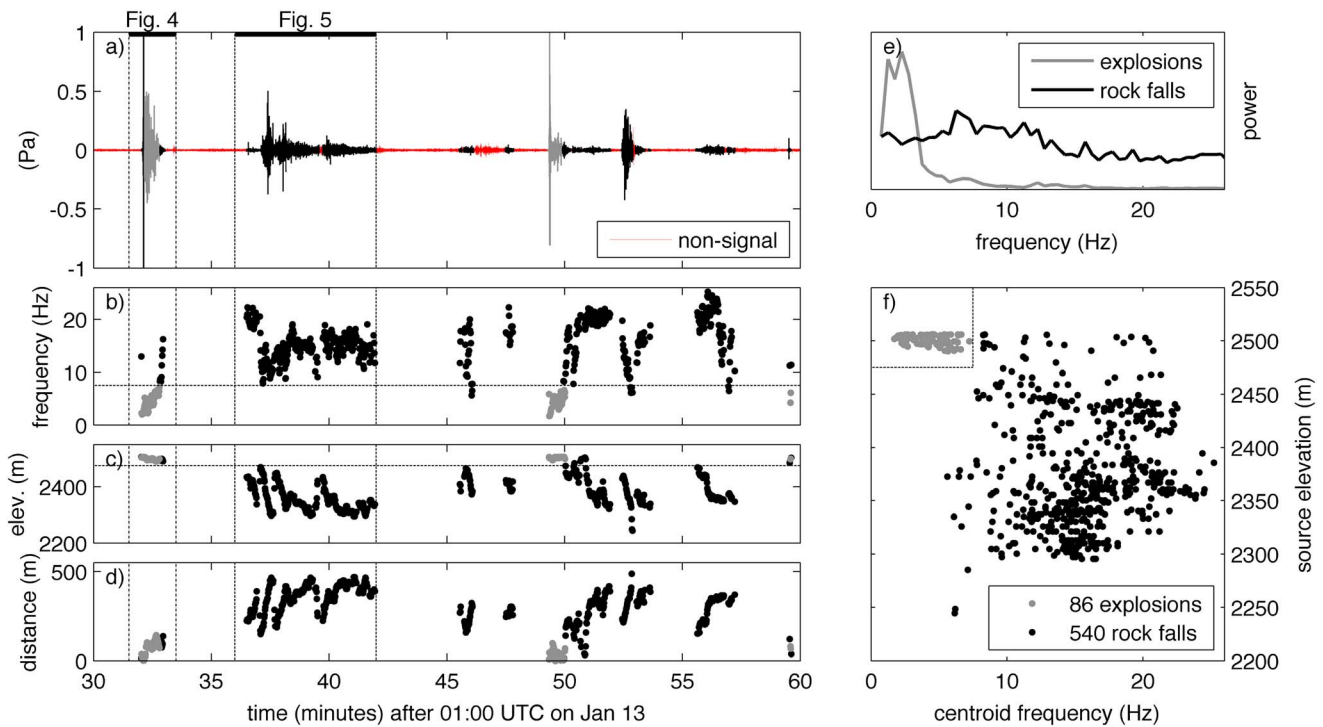
Figure 3. (a) Thirty minute time series corresponding to Figure 2 and data classified as explosion (gray), rockfall (black), and nonsignal (red) intervals. Signal 5 s time windows are indicated with their (b) centroid frequencies, (c) source elevations, and (d) vent-source distances. (e) Median power spectra for all 86 explosion and 540 rockfall windows are shown for the 30 min of data. (f) Scatterplot of elevation-frequency distribution for all signal time windows. Dashed line indicates classification domains separating explosion and rockfall events.

volcano. The locations of sources are also quantified in terms of their distance from the summit/vent and their elevation projected along the southeast ridge (Figures 3c, 3d, and 3f). The frequency content of the corresponding SNR spectrum is summarized by its centroid frequency $f_c(t)$ (Figures 3b and 3f).

The clustering of centroid frequency versus source elevation (Figure 3f) intimates two distinct event types. Those events occurring near to the summit and dominated by low frequencies are inferred to have association with explosions and/or vent degassing, while higher-frequency events occurring farther from the summit are inferred rockfalls. Median normalized spectra for the presumed explosions and rockfalls reveal characteristic spectral content (Figure 3e). Rockfalls possess higher centroid frequency (typically ~15 Hz) and are substantially more broadband than explosion signals, which possess centroid frequencies of ~5 Hz.

Details of example explosion and rockfall signal are provided in Figures 4 and 5, respectively. SNR spectral power for the explosion is clearly concentrated at lower frequencies compared to rockfalls. Cross-correlation lag times are also relatively nonvarying for the explosion, indicating a largely nonmoving source, whereas rockfall signals exhibit time lag variation due to a changing source location. The example of Figure 5 shows several pulses with similar evolution in lag times. The systematic lag time evolution suggests repeated rockfalls moving in the same manner and following similar trajectories. Cross-correlation time lag data computed from the three infrasound channels (e.g., Figures 2f, 4f, and 5f) are used to construct maps of dynamic source locations (refer to Appendix B).

Time-evolving locations of the largest rockfall event in Figure 5 (beginning at 01:37 UTC) are detailed in Figure 6. Though source location polygons (Figure 6a) provide generally poor radial resolution (i.e., in the direction from array to volcano), limited distance constraints are possible due to the fact that array beam back projection is slightly oblique to the volcano's slopes. Azimuths from the array to the sources are much better resolved because presumed rockfalls sweep through a range of compass directions. First-hand observations during the field campaign indicate that most rockfall descended close to Caliente's southeast skyline. For this reason the source "epicenter" (star symbols in Figure 6a) is taken where the lowest residual intersects the southeast ridge.
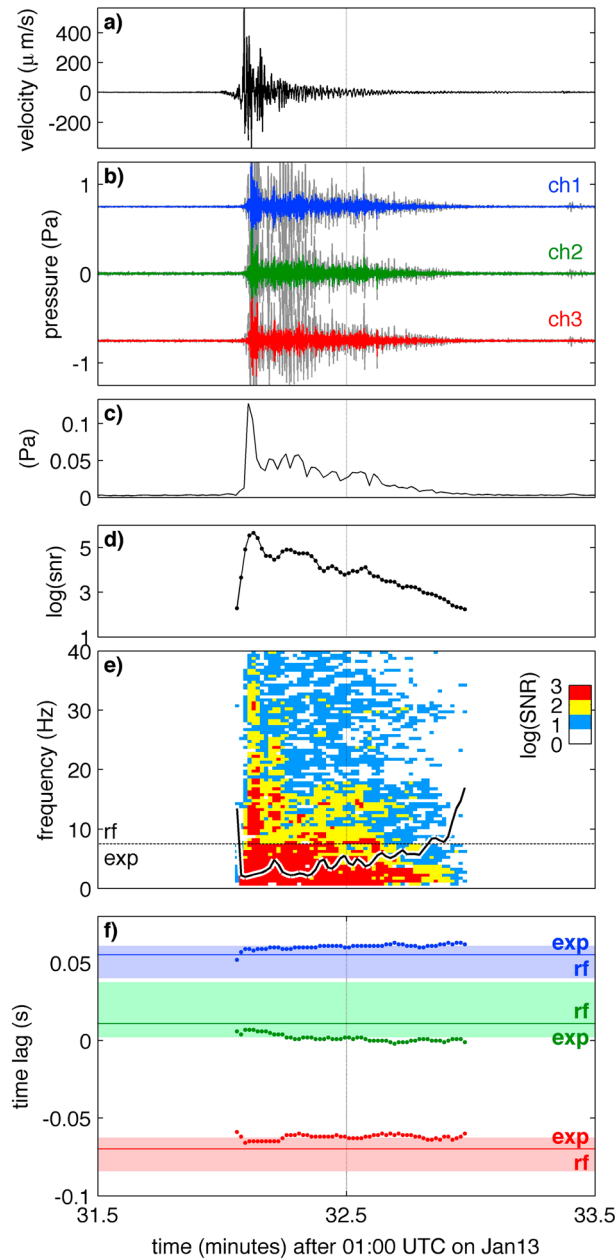
Figure 4. Two minute detail of explosion event. Caption is same as that for Figure 2.

5.2. Tracking Activity Over Extended Time Periods

Projected locations of infrasound sources on to the Caliente dome, coupled with the signals' frequency content, provide a robust means to track and classify explosions and rockfalls during extended monitoring. Although our campaign deployment at Santiaguito was brief in 2014, it provided short-term statistics on the relative occurrence rates of various events and demonstrated important proof of concept for this type of monitoring (Figure 7). These results show that a quantitative chronology of explosions and rockfall, afforded by acoustic array monitoring, could be especially useful for identifying systematic changes in the state of unrest. While this analysis corresponds to a short study interval and stable activity, long-term rockfall monitoring could be used as a proxy for changes in lava effusion rates, which are challenging to measure at Santiaguito with precision [e.g., *Harris et al.*, 2003].

Rockfall detections, and their relationship to explosion occurrence, are summarized in the hour-long records of Figure 7. As many as two explosions per hour are identified (in keeping with observations of previous studies [e.g., *Sanderson et al.*, 2010]), while more than 12 rockfalls per hour are detected during periods of elevated activity (e.g., hour 01:00 on 13 January). Such activity corresponds to about 2 cumulative minutes of explosion infrasound and ~10 cumulative minutes of rockfall infrasound during this hourly period. These results are compatible with first-hand observations of activity during the field campaign.
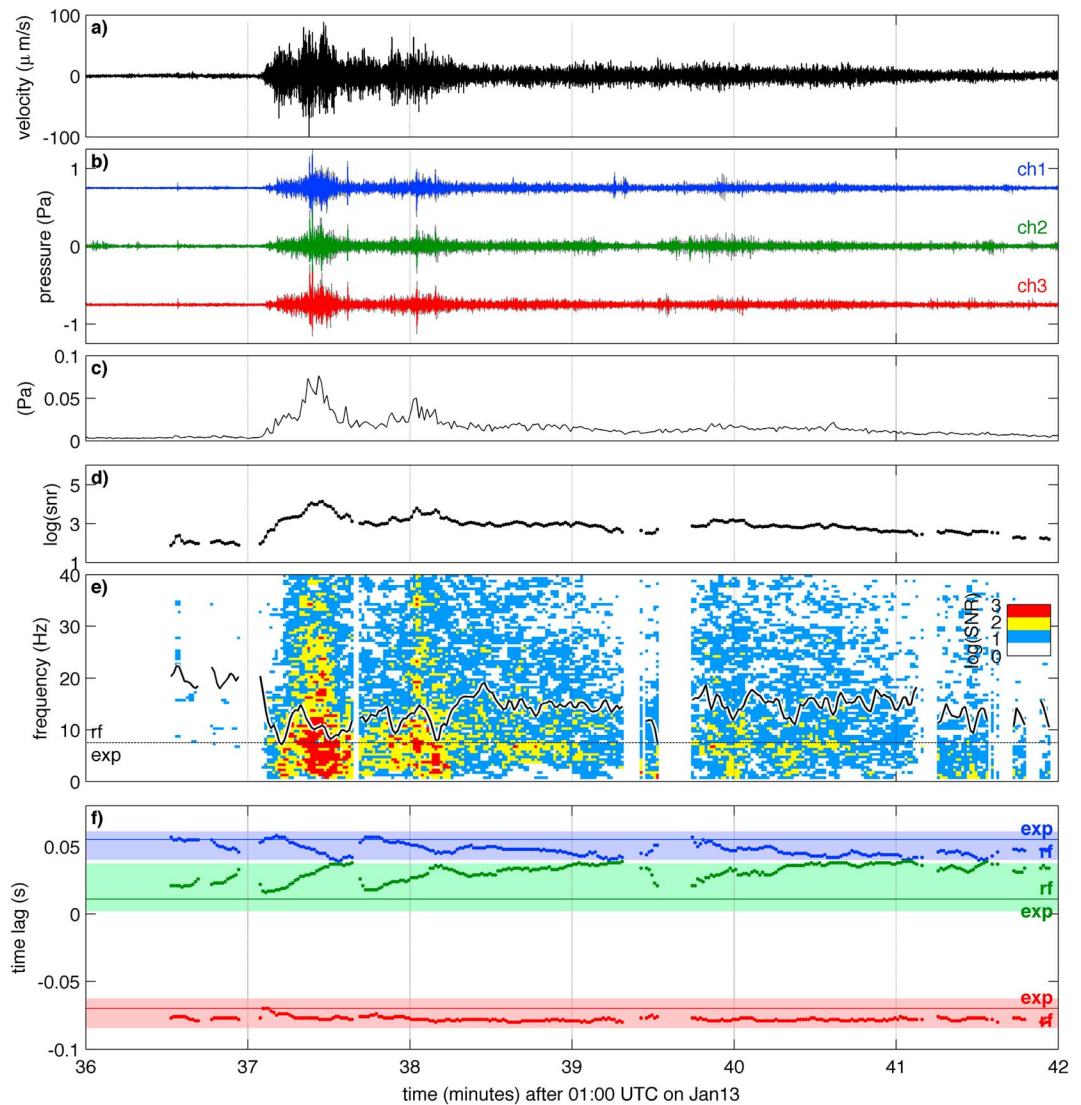
Fewer detections are evident at some other times, and their paucity is either related to less frequent activity or enhanced background infrasound band noise that obscures signal. Based upon infrasound data and video starting at 16:00 UTC on 13 January, we conclude that many of the small rockfall events are hidden by wind, which induces relatively high background noise. Wind noise obscured the detection of small rockfall events identified on video at times 16:20, 16:23, 16:50, and 16:54. Noise levels can be approximated by quantifying the difference, or dissimilarity, between the recordings on the small aperture array. The gray shading in Figure 7 is proportional to mean differenced infrasound amplitudes and is presented here as a qualitative proxy for nonvolcanic signal, or noise:

$$\bar{p}(t) = 1/3 \int_{t-5}^{t+5} |\delta p_2(t) - \delta p_1(t + \Delta t_{21})| + |\delta p_3(t) - \delta p_2(t + \Delta t_{32})| + |\delta p_1(t) - \delta p_3(t + \Delta t_{13})| \mathrm{d}t. \qquad (4)$$

Figure 5. Six minute detail of rockfall sequence. Caption is same as that for Figure 2.

Here Δt_{ij} corresponds to expected time delay between acoustic phases recorded at a channel pair assuming signal originating at, or near, the vent, i.e., $\Delta t_{21}(\text{vent}) = 0.05$, $\Delta t_{32}(\text{vent}) = 0.03$, $\Delta t_{13}(\text{vent}) = -0.08$ s.

6. Discussion

6.1. Conjoint Video and Infrasound Observation

Conjointly acquired video serves to illuminate the source processes associated with rockfall-induced infrasound. Video was collected during a subset of the infrasound campaign including during 80 min on 12 January (12:40 through 14:00 UTC) and 4.5 h on 13 January (13:30 through 18:00 UTC). Camera fields of view for the two periods were set at 32° and 60°, respectively. These two angular ranges correspond to diagonal image dimensions of 570 m and 1150 m at the distance of the volcano vent (refer to Appendix C).

Our video observations correspond to relatively typical periods of Santiaguito activity, which include one or two hourly explosions and as many as a dozen small rockfall events per hour (refer to Figure 7). Large rockfall sequences, such as the half hour featured in Figure 2 and a probable pyroclastic density current, occurring at 03:45 UTC on 12 January, were not recorded with the camera. The sources corresponding to these signals must be inferred by examining and comparing similar infrasound records for which coincident video is available.
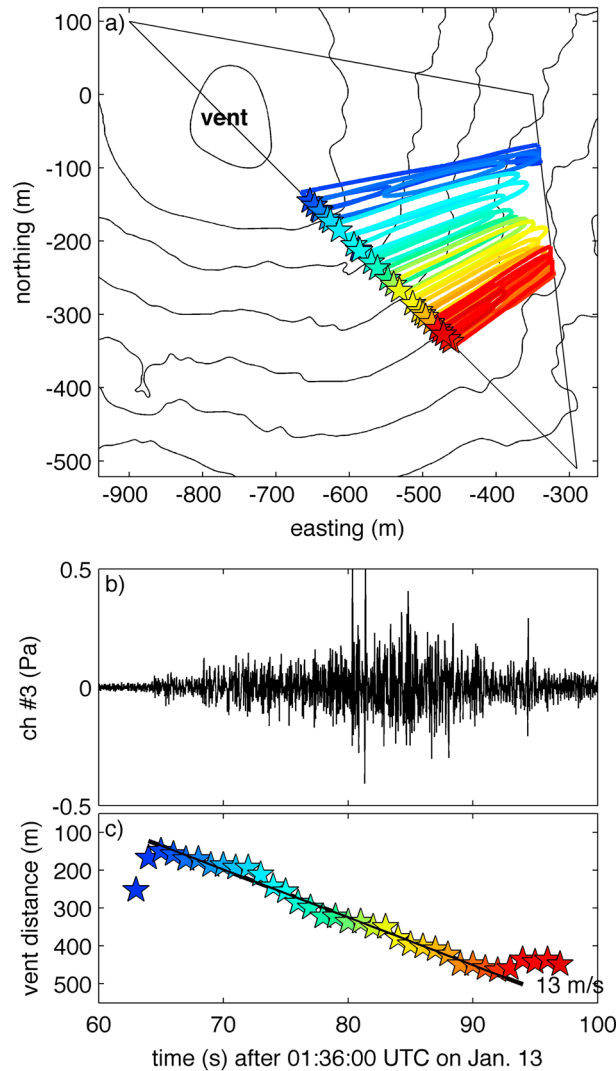
Figure 6. (a) Example rockfall signal showing translation of source locations projected onto the southeast ridge. Each polygon contour corresponds to a 4 ms timing residual for 5 s overlapping windows (equation (B2)). Star symbols correspond to the intersection of the lowest residual value with the southeast ridge. (b) Corresponding infrasound signal recorded on channel 3 and filtered in to the 4–24 Hz band. (c) Slant distance between vent/summit and sound source. Colored symbols indicate a common time basis.

Infrasound and its associated source locations are superimposed on video and given in the supporting information. Example annotated video frames from the animations are shown in Figure 8. These images and animations were created from the video decimated to 1 s and synchronized with their associated infrasound sources. Image frames are associated with infrasound waves propagating to the array with travel times of ~1–3 s. These times correspond to a range of distances for sources originating within the triangular search area *R*, located ~300 to 1000 m from the array.

Annotated images show inferred source polygons derived from ~5 s long infrasound signal. For example, supposing a video still frame captures an impulsive source initiating at 12:00:00, its sound will reach the array at about 12:00:02. This pulse, or event, could thus be detected in a range of 5 s signal windows including those starting between ~11:00:57 and ~12:00:02. Mapped source polygons thus have as much as a 5 s timing ambiguity. The animations and Figures 8e and 8f show image frame timing synchronized with both a dashed red line and with solid lines. The solid lines bracket the infrasound start times for which that frame's activity could have been detected.

Integrated video and infrasound permit ground truthing of rockfall signal (Figure 9). The first three examples in Figure 9 correspond to events for which time-synchronized video was acquired (see support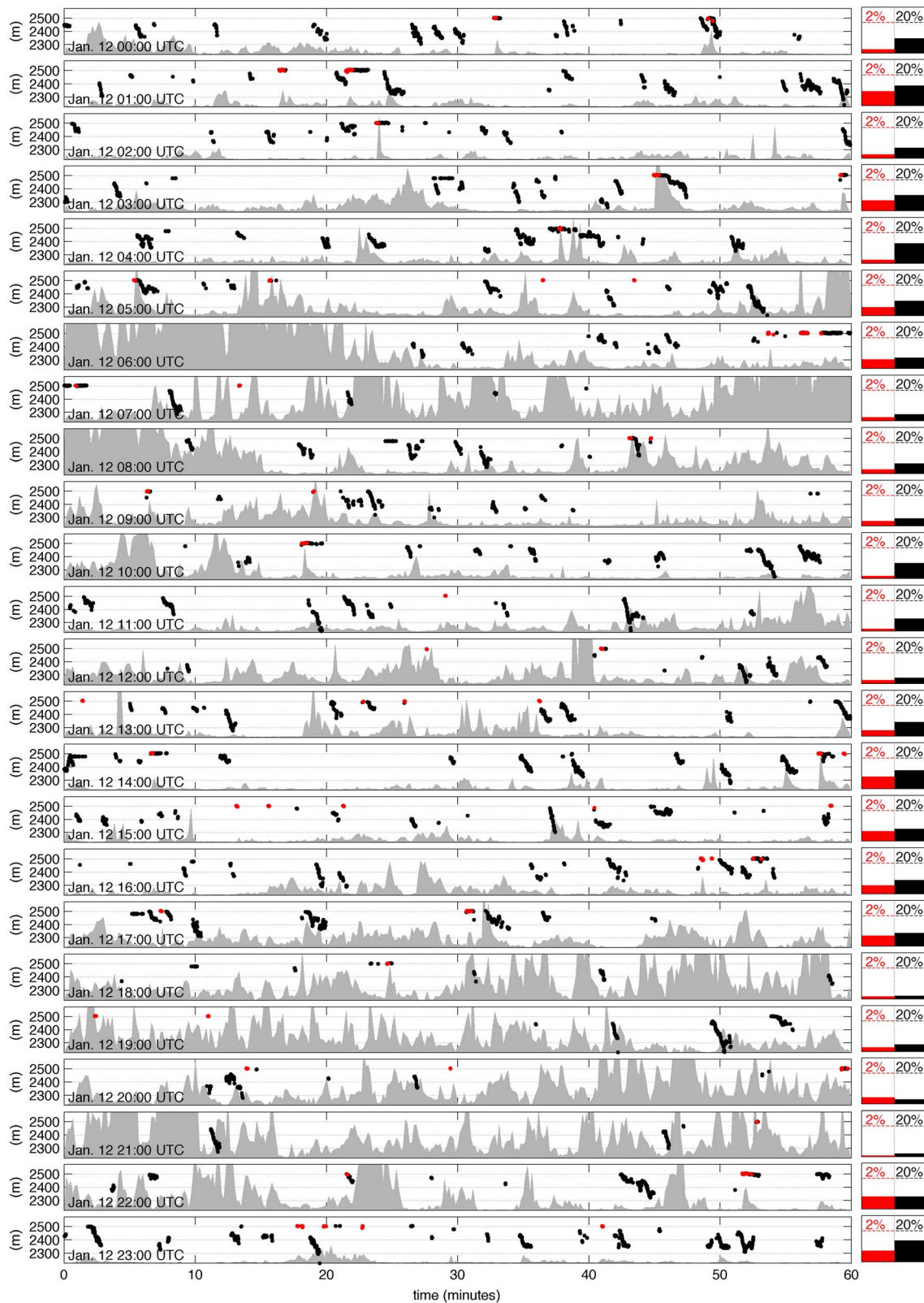ing information). From these events inferences are made to better understand cataloged signal where visual observations are unavailable. A brief description of a spectrum of Figure 9 rockfall events follows below. Flow speeds are calculated as regression fits to moving sources descending the southeast slopes. Example speeds featured in Figure 9e vary from a few m/s to nearly 10 m/s, but other measured rockfalls, including the event shown in Figure 6, indicate speeds as high as 13 m/s.

Event #1. A small rockfall with root-mean-squared infrasound pressure of ~10 mPa is detected during ~30 s. The source is tracked only for ~100 m and moves with relatively slow speeds of ~4 m/s, considerably slower than the ~15 m/s speed of an individual descending block estimated in the same video. Discrepancy in these speeds is reconciled by our hypothesis that infrasound source localization tracks the primary source of sound generation, which in this case appears to be a relatively stationary region where multiple blocks begin to spall from the scarps and travel less than 100 m before breaking up or stopping altogether. This event is an example of a moving source near the limits of infrasound detection capabilities. In the video

Figure 7. The 42 h chronology of infrasound sources located at Santiaguito during 12 January (first panel) and 13 January (second panel). Infrasound sources corresponding to inferred explosions (red) and rockfall (black) are plotted in terms of their projected elevation on the southeast ridge. Event types are classified according to the spectral and elevation criteria highlighted in Figure 3f. Histograms show hourly percentiles for which explosion and rockfall signals are identified (e.g., 10% bars correspond to 6 min of activity). Gray shading in the time series indicates 10 s averaged noise proxy according to equation (4).
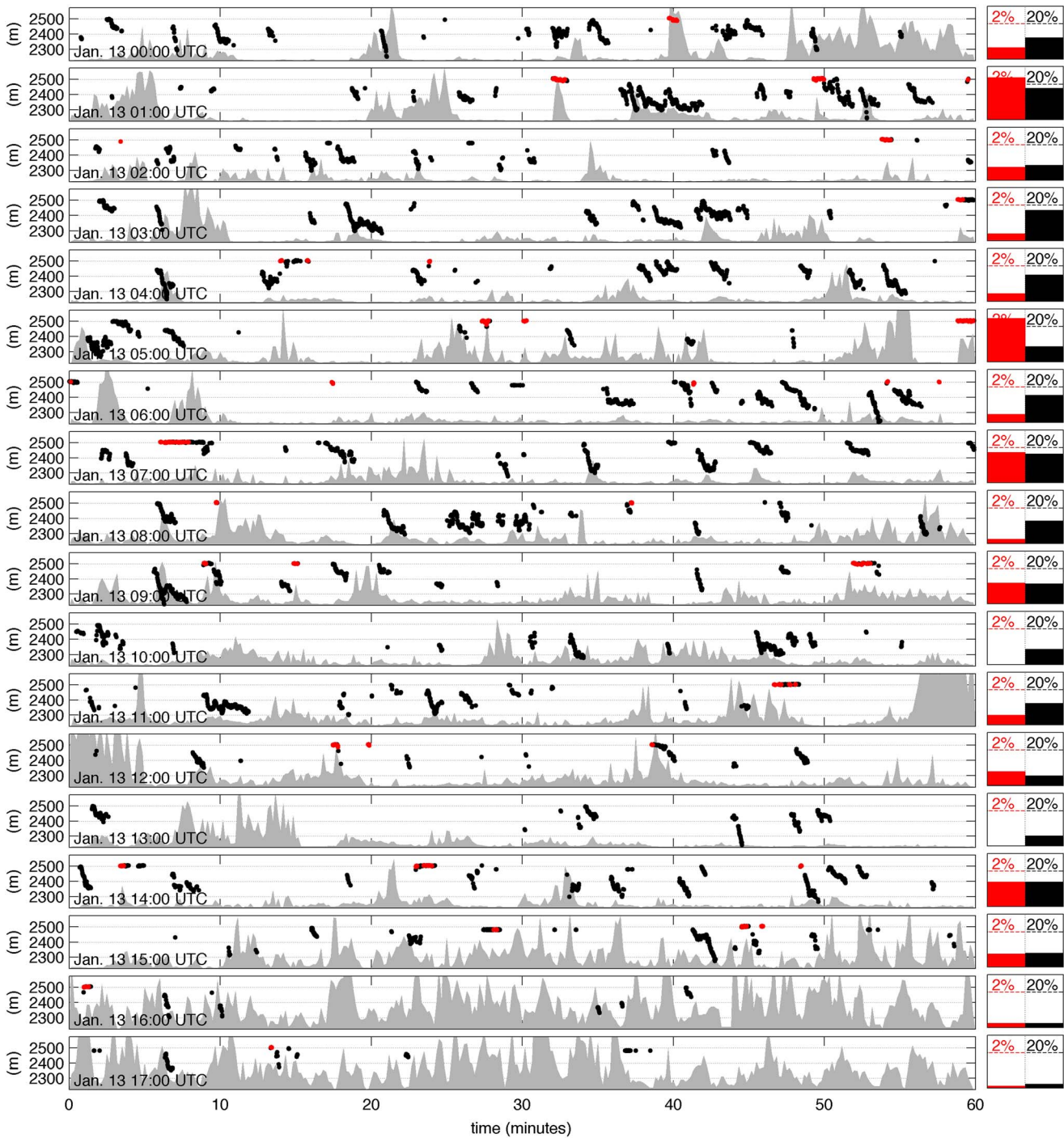
Figure 7. (continued)

only a few dozen ashy tracks are seen descending the slopes and only one of the blocks is large enough (~1 m) to be seen in more than 1 pixel on the video.

Event #2. This is a ~30 s rockfall event with greater infrasound amplitude and flow size than Event #1. It is well tracked, and its locus of sound generation moves with greater speed (~8 m/s) and substantially farther downslope than Event #1. The video corroborates the relative location of sources relative to the summit. Notably, the video also shows the event occurring on the far side of the southeast ridge skyline. Only the ash plumes kicked up by the descending blocks are visible in the video imagery. Corresponding infrasound centroid
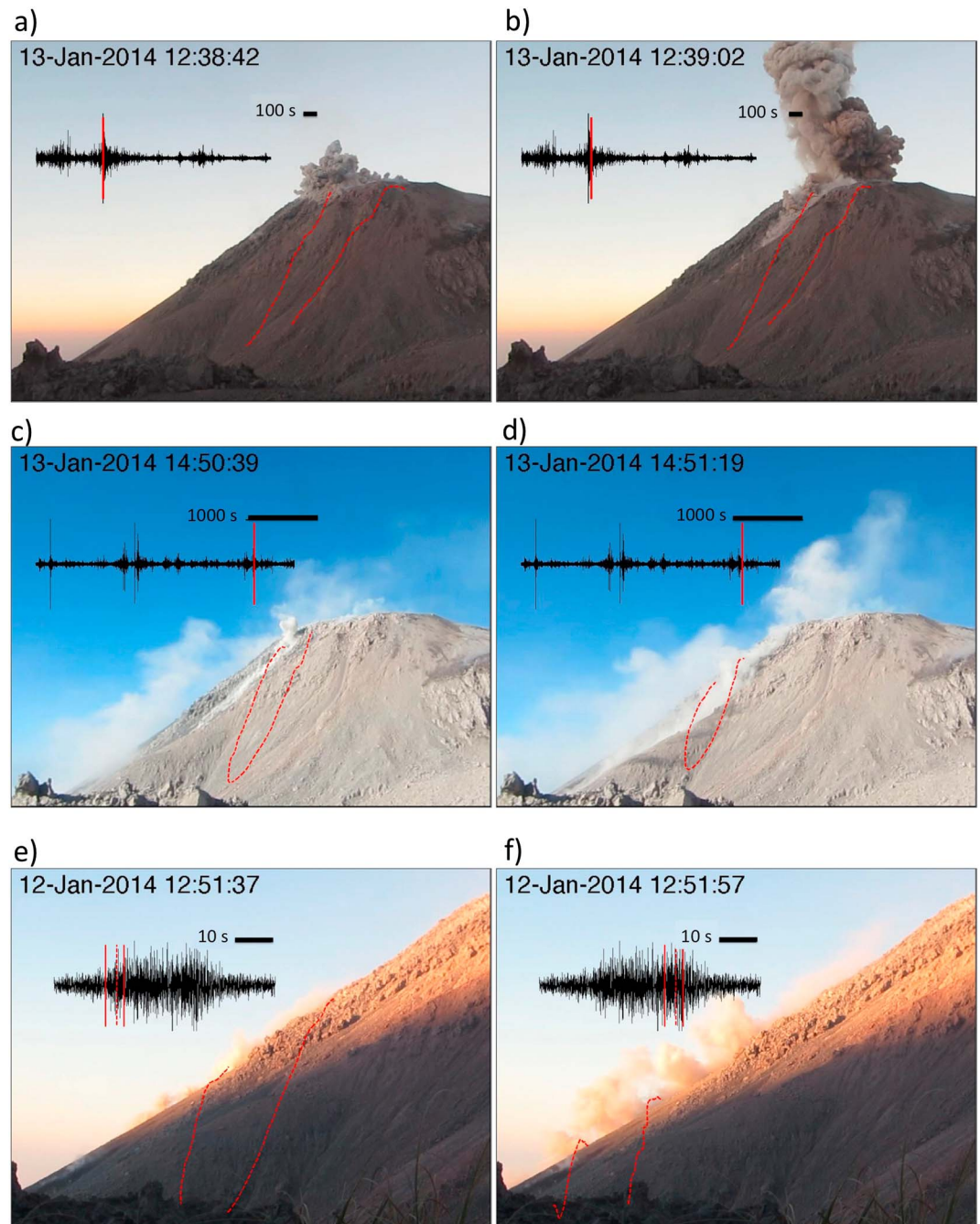
Figure 8. Select annotated images from (a–d) an hour-long period on 13 January and (e and f) a 60 s period on 12 January. These annotated images are part of Movies S1–S3 in the supporting information. Indicated events correspond to explosive eruption and small pyroclastic density current (Figures 8a and 8b), rockfall on the upper flanks on the nearside of the southeast ridge (Figures 8c and 8d), and rockfall on lower flanks just beyond the southeast ridge (Figures 8e and 8f). Image frames show source location polygons for 4 ms error residuals. Source regions correspond to ~5 s of data indicated between the solid red lines in the infrasound record. Dashed line denotes actual time of the image frame.

frequencies are relatively low for rockfall (<20 Hz) and may be affected by diffractive attenuation of infrasound as it propagates over the ridge.

Event #3. This is a high-amplitude explosion, which rapidly transitions to a higher-frequency source that moves downslope. The video confirms this moving source to be a small pyroclastic density current that "boils over" from the summit terrace and then transitions to a small rockfall. The early portion of the signal
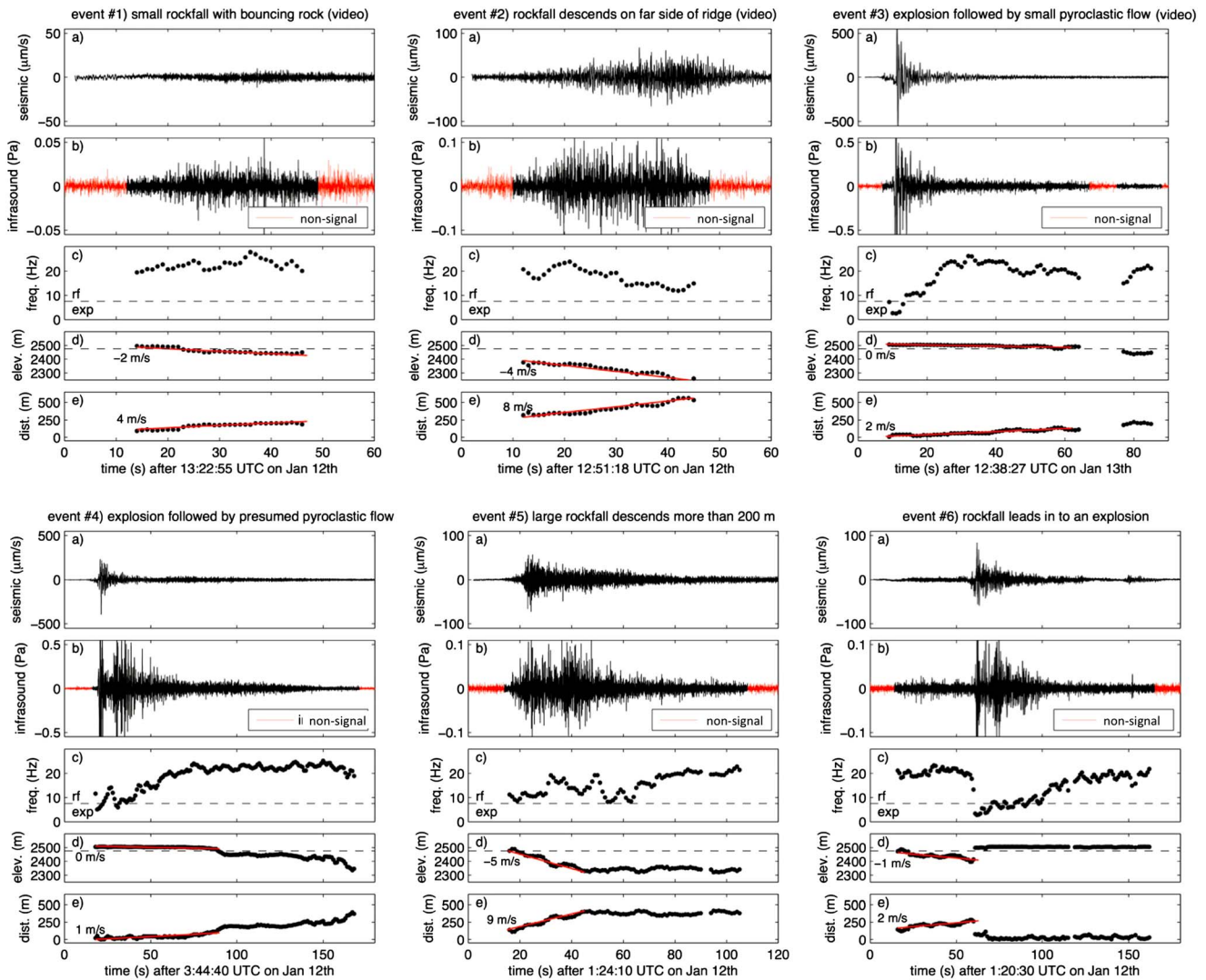
Figure 9. Events #1–6 show a variety of moving source signals. Events #1–3 are recorded with coincident video footage. Note different time scale for each event and different amplitude scales in Figures 9a and 9b. Panels for the six events are as follows: (a) unfiltered broadband seismic velocity, (b) channel 3 infrasound pressure filtered between 4 and 24 Hz, (c) centroid frequency calculated for 5 s windows with 4 s overlap, (d) inferred source elevation, and (e) slant distance from vent. Locations shown in Figures 9d and 9e assume source is confined to the southeast ridge. Source speeds are given as the slope of the linear regression (red) lines. Dashed lines in Figures 9c and 9d separate domains used to differentiate rockfall (rf) and explosions (exp).

is proximal to the vent, travels only ~100 m (see Figure 8b), and is accurately represented through infrasound source localization. The first few tens of seconds exhibit slow speed (compared to velocities shown in Figures 9d and 9e for Events #1 and #2) but high signal amplitude and a characteristic envelope that decays exponentially. These observations intimate that pyroclastic density currents may have potentially unique infrasound signatures (see also Event #4).

Event #4. This is another moving source event assumed to be a relatively large pyroclastic density current. Although there is no accompanying video, its envelope, which decays exponentially, and its location, which is near to but not at the vent, suggest similarity to *Event #3*. Its amplitude and duration are substantially larger and longer than those of Event #3, indicating a superior size. The trailing portion of the infrasound signal, which moves downslope to ~2350 m, is presumed to be rockfall.

Event #5. This is one of the largest rockfall events in terms of amplitude, vertical descent of the moving source, and signal duration. For nearly 30 s the rockfall sound generation progresses downslope before the source of sound becomes concentrated at 2300 m possibly in an accumulation zone where slope gradient decreases.

Event #6. This is a rockfall event that shows progression downslope over the course of 40 s and leads into the beginning of an explosion signal. The source location stays fixed following the explosion onset despite a systematic rise in frequencies toward higher-frequency content, which is often representative of rockfall.

6.2. Comparison of Rockfall Seismicity and Infrasound

Conjoint seismic recordings clearly indicate the appearance of many rockfall events as classical cigar-shaped high-frequency tremors with emergent onsets and signal duration comparable to the corresponding infrasound. In many cases, the seismic signature of rockfall exhibits higher signal-to-noise ratio than the infrasound counterpart (e.g., see Figure 5). This is due in part to the relatively high levels of noise present in infrasound data recorded near to a volcano, which is particularly exposed to wind. For this reason, seismic rockfall signals remain useful for event counting during high winds and/or when other noise might inhibit infrasound signal detection.

Although seismic waveforms may have a "cleaner" appearance than their infrasound counterparts, their capability for locating small amplitude transients is limited for a variety of reasons. Heterogeneities within the solid volcano, including structures with velocity contrasts, will contribute to seismic wave scattering and multipathing. The source time functions of rockfall tractions thus become distorted and extended in duration, as recorded by seismic stations. Events #1 and #2 in Figure 9 show seismic rockfall energy that appears delayed with respect to the infrasound recordings. Complicated Green's functions may also inhibit the capabilities of a seismic array for precise timing and localization of extended duration sources [*Almendros et al.*, 2002; *Chouet et al.*, 1998]. Finally, seismic velocities and wavelengths are generally an order of magnitude greater than infrasound speeds and signal wavelengths and contribute to relatively diminished seismic source location precision.

7. Conclusion

Despite potentially high levels of noise inherent in infrasound data, a single array proves remarkably effective for detecting small rockfall events. The proximal Santiaguito three-element array is shown to be adequate for tracking and quantifying the timing, size, and distance traveled by these flows. This study has outlined a simple processing procedure for locating moving sources in a geographically restricted search area. Such monitoring has clear hazard mitigation application for tracking rockfall and pyroclastic density current movement at any active volcano.

We have shown that precise location of Santiaguito rockfall sources is limited by the geometry of the array with respect to the zone of active rockfall. In future studies ambiguity of source location in the radial direction could be mitigated by the deployment of dual arrays. Potentially, multiple arrays and arrays with more than three sensors could be used to detect and track even smaller transients and/or a greater quantity of events when ambient noise is high.

Appendix A: Processing (Signal Identification)

For a discrete data window starting at time *t*, the signal is defined by highly correlated and consistent travel time delays between the three independent sensor pairs. In our study consistency is met when the sum of phase lags is less than 1 ms, i.e.,

$$C(t) = |\Delta\tau_{21}(t) + \Delta\tau_{32}(t) + \Delta\tau_{13}(t)| \leq 0.001 \, \text{s}. \tag{A1}$$

Here the subscripts indicate channel number and $\Delta\tau_{ji}$ denotes the computed lag time delay associated with peak cross correlation between channels *j* and *i*. A time-varying cross-correlation matrix is computed at 1 s time steps and for windows of 5 s (i.e., 500 samples) starting at time *t*.

$$\left[\phi_{ij}(t)\right]_k = \sum_{s}^{s+499} \left[\partial p_i(t)\right]_s \left[\partial p_j(t)\right]_{s+k}. \tag{A2}$$
$$\scriptstyle k\in[-20,20]$$

Excess pressure ∂p in this rockfall study is band-pass (4–24 Hz) filtered infrasound. The time window starting at *t* (in seconds) corresponds to the sample interval [*s*, *s* + 499] where the starting samples are $s(t) = t \times 100$. Peak cross-correlation time lags are considered only within a range of discrete phase delays of $k \in [-20, 20]$
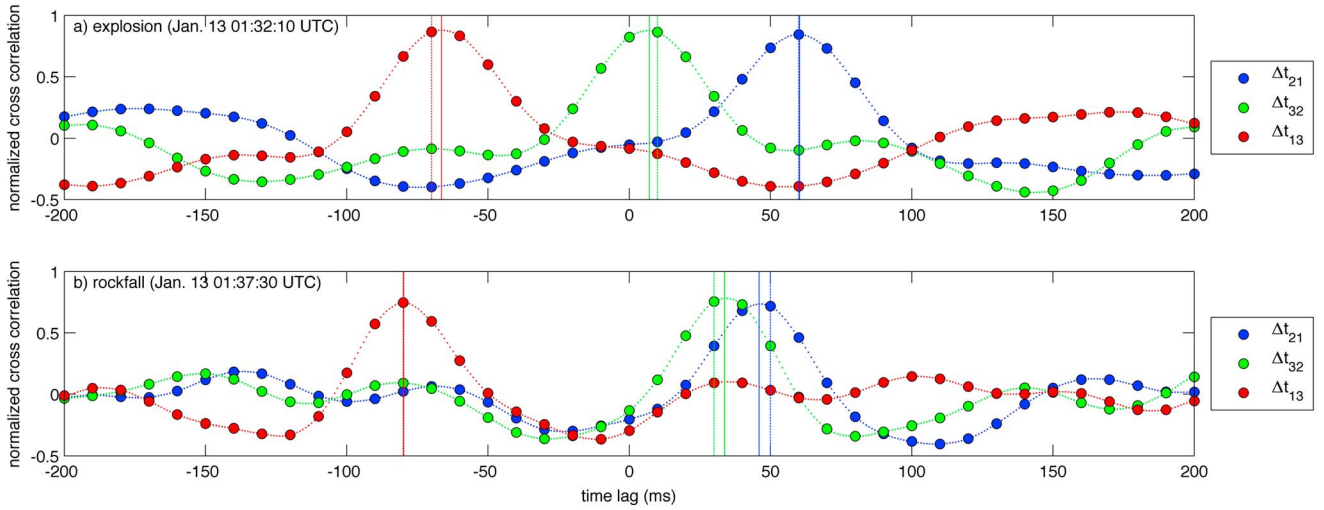
Figure A1. Examples of well-correlated (a) explosion signal and (b) rockfall signal showing cross-correlation series and phase lag picks. Cross correlations of original 100 Hz data are indicated with large colored circles for the three station pairs. Cross correlations for interpolated 1000 Hz data are shown with small colored dots. Dashed and solid vertical lines indicate 0.01 and 0.001 s resolution lag time picks, respectively.

samples (i.e., ±0.2 s), which is about a factor of 2 longer than the maximum expected acoustic phase delays for a ~30 m aperture array.

$$\Delta \tau_{ij}(t) = \arg \max_{k \in [-20, 20]} \left[\phi_{ij}(t) \right]_k .$$ (A3)

Phase lags $\Delta \tau_{ji}$ are only calculated for those time windows that are consistent and possess maximum normalized cross-correlation values in excess of 0.5 for all three channel pairs, i.e.,

$$\left[\Phi_{ij}(t) \right] = \frac{1}{499} \frac{\sum\limits_{s}^{s+499} [\partial p_i]_s [\partial p_j]_{s+\Delta \tau_{ij}}}{\sqrt{\sum\limits_{s}^{s+499} \left([\partial p_i]_s \right)^2} \sqrt{\sum\limits_{s}^{s+499} \left([\partial p_j]_{s+\Delta \tau_{ij}} \right)^2}} \geq 0.5 .$$ (A4)

Time-varying phase lags $\Delta \tau_{ij}(t)$ indicate moving sources, but resolution of source back azimuth is limited to the sample rate of the digitized infrasound time series. In order to improve upon the initial sampling resolution of 0.01 s (100 Hz), we resample the cross-correlation functions $[\phi_{ij}]_k$ by a factor of 10 using cubic interpolation. Upsampling to achieve better location resolution has precedence in seismic data analysis and can be done in both the time and frequency domains [e.g., *Fremont and Malone*, 1987]. Figure A1 shows infrasound signal with correlation phase lags of both the original data (sample at 100 Hz) and resampled data at 1000 Hz. Phase lag refinement is indicated by the offsets in the vertical solid and dashed lines. The peak correlation phase picks at 1000 Hz (solid lines) are used in the time series in Figures 2f, 4f, and 5f and for subsequent source localization.

Appendix B: Processing (Source Localization and Errors)

Upsampled (1000 Hz) phase time lags $\Delta \tau_{ij}(t)$ calculated from correlated infrasound data are compared against predicted, or modeled, time lags to map source location likelihood. Modeled time lags are calculated within the restricted search area R and confined to the surface of the digital elevation model, where volcanic events are expected. For the short transit distances relevant to this study we assume straight-line propagation of sound between sources at x, y, z and the acoustic sensor locations within the array, x_i, y_i, z_i and x_j, y_j, z_j. We calculate an estimated phase lag associated with each candidate source location as follows:

$$\Delta t_{ij}(x, y, z) = \frac{1}{c} \left[\sqrt{(x - x_j)^2 + (y - y_j)^2 + (z - z_j)^2} - \sqrt{(x - x_i)^2 + (y - y_i)^2 + (z - z_i)^2} \right],$$ (B1)

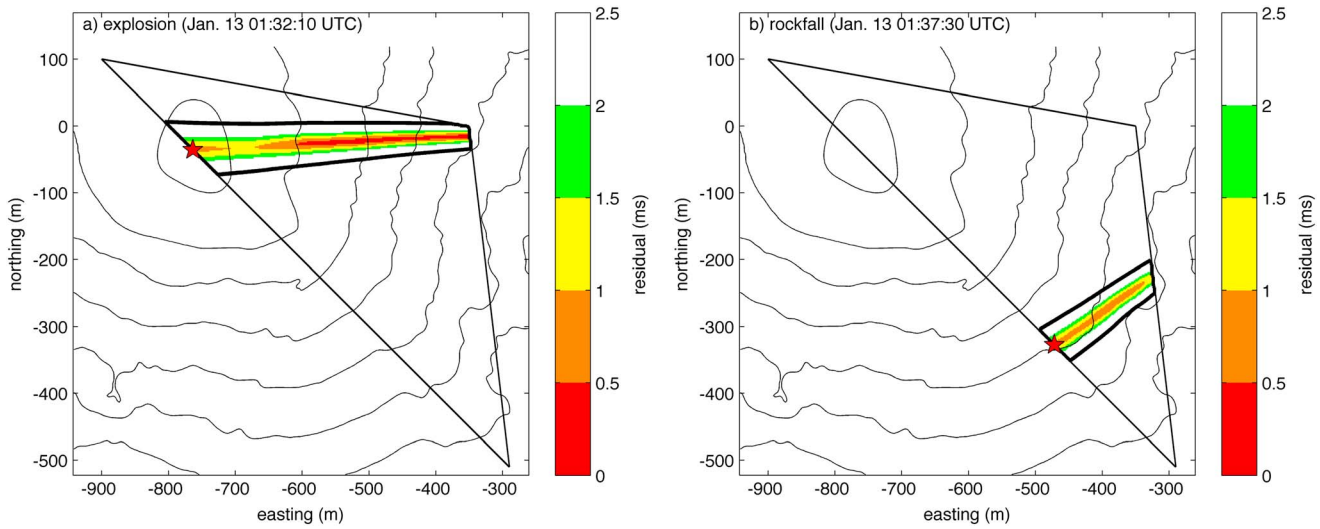**Figure B1.** Acoustic source location maps plotted in terms of residual (ε) for (a) an explosion and (b) a rockfall example for 5 s signal windows. Star indicates the minimum value of epsilon, which lies on the southeast ridge. The 4 ms residual is shown as a thick black line.

where intrinsic sound speed c is fixed at 343 m/s, which is appropriate for 20°C. A range of possible sound speeds ranging from 338 to 349 m/s (10°C to 30°C) provides only a minimal (less than few meters) impact on inferred source location.

Timing residuals are quantified as the l^2-norm root-mean-squared misfit between predicted lag delays and cross-correlation time delays as follows:

$$\varepsilon(x, y, z, t) = \sqrt{\left(\Delta\tau_{21}(t) - \Delta t_{21}\right)^2 + \left(\Delta\tau_{31}(t) - \Delta t_{31}\right)^2 + \left(\Delta\tau_{13}(t) - \Delta t_{13}\right)^2}. \quad \text{(B2)}$$

These residual values are then mapped as contours in plan view to identify probable source locations and also provide insight into location error (Figure B1). Broad regions of low residual suggest either spatial uncertainty or distributed source regions. In this study the principle axis of uncertainty lies along the radial direction. For example, in Figures B1a and B1b the 4 ms residual contour provides no constraint in the radial direction but yields a precision of about 50 m in the tangential direction. Because of the radial uncertainty, we identify source locations as the coordinate, x_l, y_l, z_l, on the southeast ridge with minimum residual.

$$[x_l(t), y_l(t), z_l(t)] = \underset{x_l, y_l \in [\text{SE ridge}]}{\arg\min}[\varepsilon(t)] \quad \text{(B3)}$$

The southeast ridge and nearby slopes correspond to field observations of nearly all Santiaguito's rockfalls.

Appendix C: Mapping Sources Locations to Image Frames

Locations of the digital terrain are roughly projected on to the video still images (e.g., Figures 1 and 8 and supporting information Movies S1–S3). Digital elevation model coordinates x, y, z are converted to camera look azimuth θ and elevation angle α for the known camera location x_c, y_c, z_c where

$$\theta = \tan^{-1}\left(\frac{x - x_c}{y - y_c}\right) \quad \text{(C1)}$$

and

$$\alpha = \tan^{-1}\left(\frac{z - z_c}{\sqrt{(y - y_c)^2 + (x - x_c)^2}}\right). \quad \text{(C2)}$$

Map features, such as the boundaries of R or located infrasound sources, can then be projected on to video frames. First, image resolution is inferred for camera focal length and image pixel density. For the featured
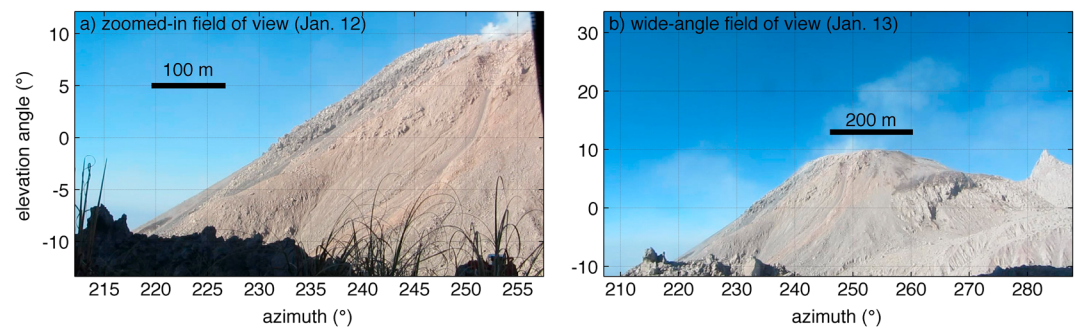
Figure C1. Image registration in terms of camera look direction and elevation angle for (a) zoomed-in views on 12 January and (b) wide-angle views on 13 January. Bars denote inferred scaling at an approximate camera-vent distance of ~900 m.

imagery the angular field of view per pixel was 0.035° and 0.063° for wide and zoomed-in images, respectively. Next, registration of an image is accomplished by fixing the visible summit of Caliente to its known look azimuth ($\theta = 253°$) and elevation angle ($\alpha = 10°$). Figure C1 shows zoomed-in and wide-angle images with horizontal and vertical axes annotated in terms of view angle. Potential camera image distortion or vignetting is not accounted for when projecting mapped features on to these image frames. As such, overlay of infrasound source locations should be considered as an approximation of their actual location on the image.

References

Almendros, J., B. Chouet, P. B. Dawson, and C. Huber (2002), Mapping the sources of the seismic wave field at Kilauea volcano, Hawaii, using data recorded on multiple seismic antennas, *Bull. Seismol. Soc. Am.*, *92*(6), 2333–2351, doi:10.1785/0120020037.

Bluth, G. J. S., and W. I. Rose (2004), Observations of eruptive activity at Santiaguito volcano, Guatemala, *J. Volcanol. Geotherm. Res.*, *136*(3–4), 297–302, doi:10.1016/j.jvolgeores.2004.06.001.

Cannata, A., P. Montalto, E. Privitera, G. Russo, and S. Gresta (2009), Characterization and location of infrasonic sources in active volcanos: Mt. Etna, September–November 2007, *J. Geophys. Res.*, *114*, B08308, doi:10.1029/2008JB006007.

Chouet, B. A., P. B. Dawson, G. De Luca, M. Martini, G. Milana, G. Saccorotti, and R. Scarpa (1998), Array analyses of seismic sources at Stromboli, *Acta Vulcanol.*, *10*(2), 367–382.

Delle Donne, D., M. Ripepe, S. De Angelis, P. D. Cole, G. Lacanna, P. Poggi, and R. Stewart (2014), Chapter 9 Thermal, acoustic and seismic signals from pyroclastic density currents and vulcanian explosions at Soufriere Hills Volcano, Montserrat, *Geol. Soc. London Mem.*, *39*, 169–178, doi:10.1144/M39.9.

Fee, D., and R. S. Matoza (2013), An overview of volcano infrasound: From Hawaiian to Plinian, local to global, *J. Volcanol. Geotherm. Res.*, *249*, 123–139, doi:10.1016/j.jvolgeores.2012.09.002.

Fee, D., A. Yokoo, and J. B. Johnson (2014), Introduction to an open community infrasound dataset from the actively erupting Sakurajima Volcano, Japan, *Seismol. Res. Lett.*, *85*(6), 1151–1162, doi:10.1785/0220140051.

Fremont, M. J., and S. D. Malone (1987), High-precision relative locations of earthquakes at Mount St. Helens, Washington, *J. Geophys. Res.*, *92*(B10), 10,223–10,236, doi:10.1029/JB092iB10p10223.

Garces, M., A. Harris, C. Hetzer, J. Johnson, S. Rowland, E. Marchetti, and P. Okubo (2003), Infrasonic tremor observed at Kilauea Volcano, Hawai'i, *Geophys. Res. Lett.*, *30*(20), 2023, doi:10.1029/2003GL018038.

Harris, A. J. L., W. I. Rose, and L. Flynn (2003), Temporal trends in lava dome extrusion at Santiaguito, 1922–2000, *Bull. Volcanol.*, *65*, 77–89, doi:10.1007/s00445-002-0243-0.

Hibert, C., A. Mangeney, G. Grandjean, and N. M. Shapiro (2011), Slope instabilities in Dolomieu crater, Reunion Island: From seismic signals to rockfall characteristics, *J. Geophys. Res.*, *116*, F04032, doi:10.1029/2011JF002038.

Johnson, J. B., and J. M. Lees (2010), Sound produced by the rapidly inflating Santiaguito lava dome, Guatemala, *Geophys. Res. Lett.*, *37*, L22305, doi:10.1029/2010GL045217.

Johnson, J. B., and J. L. Palma (2015), Lahar infrasound associated with Villarrica's 3 March 2015 eruption, *Geophys. Res. Lett.*, *42*, 6324–6331, doi:10.1002/2015GL065024.

Johnson, J. B., and M. Ripepe (2011), Volcano infrasound: A review, *J. Volcanol. Geotherm. Res.*, *206*, 61–69, doi:10.1016/j.jvolgeores.2011.06.006.

Johnson, J. B., J. J. Lyons, B. J. Andrews, and J. M. Lees (2014), Explosive dome eruptions modulated by periodic gas-driven inflation, *Geophys. Res. Lett.*, *41*, 6689–6697, doi:10.1002/2014GL061310.

Jolly, A. D., G. Thompson, and G. E. Norton (2002), Locating pyroclastic flows on Soufriere Hills Volcano, Montserrat, West Indies, using amplitude signals from high dynamic range instruments, *J. Volcanol. Geotherm. Res.*, *118*(3–4), 299–317, doi:10.1016/S0377-0273(02)00299-8.

Jones, K. R., and J. B. Johnson (2011), Mapping complex eruptive activity at Santiaguito, Guatemala using network infrasound semblance, *J. Volcanol. Geotherm. Res.*, *199*, 15–24, doi:10.1016/j.jvolgeores.2010.08.006.

Luckett, R., B. Baptie, and J. Neuberg (2002), The relationship between degassing and rockfall signals at Soufriere Hills Volcano, Montserrat, *Geol. Soc. London Mem.*, *21*, 595–602, doi:10.1144/GSL.MEM.2002.021.01.28.

Marcillo, O., J. B. Johnson, and D. Hart (2012), Implementation, characterization, and evaluation of an inexpensive low-power low-noise infrasound sensor based on a micro-machined differential pressure transducer and a mechanical filter, *J. Atmos. Oceanic Technol.*, *29*, 1275–1284, doi:10.1175/JTECH-D-11-00101.1.

Matoza, R., A. E. Hedlin, and M. Garces (2006), An infrasound array study of Mount St. Helens, *J. Volcanol. Geotherm. Res.*, *160*, 249–262, doi:10.1016/j.jvolgeores.2006.10.006.

Moran, S. C., R. Matoza, M. Garces, A. E. Hedlin, D. Bowers, W. E. Scott, D. R. Sherrod, and J. W. Wallace (2008), Seismic and acoustic recordings of an unusually large rockfall at Mount St. Helens, Washington, *Geophys. Res. Lett.*, *35*, L19302, doi:10.1029/2008GL035176.

Norris, R. D. (1994), Seismicity of rockfalls and avalanches at three cascade volcanoes: Implications for seismic detection of hazardous mass movements, *Bull. Seismol. Soc. Am.*, *84*(6), 1925–1939.

Olson, J., and C. Szuberla (2008), Processing infrasonic array data, in *Handbook of Signal Processing in Acoustics*, edited by M. Vorlander, pp. 1487–1496, Springer, New York, doi:10.1007/978-0-387-30441-0_81.

Oshima, H., and T. Maekawa (2001), Excitation process of infrasonic waves associated with Merapi-type pyroclastic flow as revealed by a new recording system, *Geophys. Res. Lett.*, *28*(6), 1099–1102, doi:10.1029/1999GL010954.

Ripepe, M., et al. (2009), Tracking pyroclastic flows at Soufriere Hills Volcano, *Eos Trans. AGU*, *90*, 229–230, doi:10.1029/2009EO270001.

Rose, W. I. (1987), Volcanic activity at Santiaguito volcano, 1976–1984, *Geol. Soc. Am.*, *212*, 17–27, doi:10.1130/SPE212-p17.

Sanderson, R., J. B. Johnson, and J. M. Lees (2010), Ultra-long period seismic signals and cyclic deflation coincident with eruptions at Santiaguito volcano, Guatemala, *J. Volcanol. Geotherm. Res.*, *198*, 35–44, doi:10.1016/j.jvolgeores.2010.08.007.

Vila, J., R. Macia, D. Kumar, R. Oritz, H. Moreno, and A. M. Correig (2006), Analysis of the unrest of active volcanoes using variations of the base level noise seismic spectrum, *J. Volcanol. Geotherm. Res.*, *163*, 11–20, doi:10.1016/j.jvolgeores.2005.10.011.

Yamasato, H. (1997), Quantitative analysis of pyroclastic flows using infrasonic and seismic data at Unzen Volcano, Japan, *J. Phys. Earth*, *45*, 397–416.

Yokoo, A., Y. J. Suzuki, and M. Iguchi (2014), Dual infrasound sources from a vulcanian eruption of Sakurajima volcano inferred from cross-array observation, *Seismol. Res. Lett.*, *85*(6), 1212–1222, doi:10.1785/0220140047.